Scalable photonic crystal chips for high sensitivity protein detection

Feng Liang,[1,3] **Nigel Clarke,**[2,3] **Parth Patel,**[2] **Marko Loncar,**[2] **and Qimin Quan**[1,*]

[1] *Rowland Institute at Harvard University, Cambridge, MA 02142, USA*
[2] *School of Engineering and Applied Sciences, Harvard University, Cambridge, MA 02138, USA*
[3] *These authors contributed equally to this work.*
[*] *quan@rowland.harvard.edu*

Abstract: Scalable microfabrication technology has enabled semiconductor and microelectronics industries, among other fields. Meanwhile, rapid and sensitive bio-molecule detection is increasingly important for drug discovery and biomedical diagnostics. In this work, we designed and demonstrated that photonic crystal sensor chips have high sensitivity for protein detection and can be mass-produced with scalable deep-UV lithography. We demonstrated label-free detection of carcinoembryonic antigen from pg/mL to μg/mL, with high quality factor photonic crystal nanobeam cavities.

OCIS codes: (230.5298) Photonic crystals; (140.4780) Optical resonators; (280.1415) Biological sensing and sensors.

References and links

1. E. Engvall and P. Perlmann, "Enzyme-linked immunosorbent assay (ELISA) quantitative assay of immunoglobulin G," Immunochemistry **8**, 871–874 (1971).
2. B. K. Van Weeman and A. H. Schuurs, "Immunoassay using antigen-enzyme conjugates," FEBS Lett. **15**, 232–236 (1971).
3. D. J. Cahill, "Protein and antibody arrays and their medical applications," J. Immunol. Methods **250**, 81–91 (2001).
4. T. Kodadek, "Protein microarrays: prospects and problems," Chem. Biol. **8**, 105–115 (2001).
5. Q. Quan, P. B. Deotare, and M. Loncar, "Photonic crystal nanobeam cavity strongly coupled to the feeding waveguide," Appl. Phys. Lett. **96**, 203102 (2010).
6. K. J. Vahala, "Optical microcavities," Nature **424**, 839–846 (2003).
7. M. Loncar, A. Scherer, and Y. M. Qiu, "Photonic crystal laser sources for chemical detection," Appl. Phys. Lett. **82**, 4648–4650 (2003).
8. E. Chow, A. Grot, L. W. Mirkarimi, M. Sigalas, and G. Girolami, "Ultracompact biochemical sensor built with two-dimensional photonic crystal microcavity," Opt. Lett. **29**, 1093–1095 (2004).
9. S. Kita, K. Nozaki, and T. Baba, "Refractive index sensing utilizing a cw photonic crystal nanolaser and its array configuration," Opt. Express **16**, 8174–8180 (2008).
10. A. Di Falco, L. O'Faolain, and T. F. Krauss, "Chemical sensing in slotted photonic crystal heterostructure cavities," Appl. Phys. Lett. **94**, 063503 (2009).
11. B. W. Wang, M. A. Dundar, R. Notzel, F. Karouta, S. L. He, and R. W. van der Heijden, "Photonic crystal slot nanobeam slow light waveguides for refractive index sensing," Appl. Phys. Lett. **97**, 151105 (2010).
12. T. Xu, N. Zhu, M. Y. C. Xu, L. Wosinski, J. S. Aitchison, and H. E. Ruda, "Pillar-array based optical sensor," Opt. Express **18**, 5420–5425 (2010).
13. Q. Quan and M. Loncar, "Deterministic design of wavelength scale, ultra-high Q photonic crystal nanobeam cavities," Opt. Express **19**, 18529–18542 (2011).
14. D. Taillaert, F. Van Laere, M. Ayre, W. Bogaerts, D. Van Thourhout, P. Bienstman, and R. Baets, "Grating couplers for coupling between optical fibers and nanophotonic waveguides," Jpn. J. Appl. Phys. **45**, 6071–6077 (2006).

#199338 - $15.00 USD Received 14 Oct 2013; revised 3 Dec 2013; accepted 4 Dec 2013; published 19 Dec 2013

15. D. Yang, H. Tian, Y. Ji, and Q. Quan, "Design of simultaneous high-Q and high-sensitivity photonic crystal refractive index sensors," J. Opt. Soc. Am. B **30**, 2027–2031 (2013).
16. D. Yang, S. Kita, F. Liang, C. Wang, H. Tian, Y. Ji, M. Loncar, and Q. Quan, "High sensitivity and high Q-factor nanoslotted parallel quadrabeam photonic crystal cavity for real-time and label-free sensing," submitted.
17. F. Vollmer and S. Arnold, "Whispering-gallery-mode biosensing: label-free detection down to single molecules," Nat. Methods **5**, 591–596 (2008).
18. A. L. Washburn, L. C. Gunn, and R. C. Bailey, "Label-free quantitation of a cancer biomarker in complex media using silicon photonic microring resonators," Anal. Chem. **81**, 9499–9506 (2009).
19. J. M. Goddard and D. Erickson, "Bioconjugation techniques for microfluidic biosensors," Anal. Bioanal. Chem. **394**, 469–479 (2009).
20. S. Zlatanovic, L. W. Mirkarimi, M. M. Sigalas, M. A. Bynum, E. Chow, K. M. Robotti, G. W. Burr, S. Esener, and A. Grot, "Photonic crystal microcavity sensor for ultracompact monitoring of reaction kinetics and protein concentration," Sens. Actuators B Chem. **141**, 13–19 (2009).
21. M. Iqbal, M. A. Gleeson, B. Spaugh, F. Tybor, W. G. Gunn, M. Hochberg, T. Baehr-Jones, R. C. Bailey, and L. C. Gunn, "Label-free biosensor arrays based on silicon ring resonators and high-speed optical scanning instrumentation," IEEE Sel. Top. Quantum Electron. **16**, 654–661 (2010).
22. M. G. Scullion, A. Di Falco, and T. F. Krauss, "Slotted photonic crystal cavities with integrated microfluidics for biosensing applications," Biosens. Bioelectron. **27**, 101–105 (2011).
23. S. Pal, E. Guillermain, R. Sriram, B. L. Miller, P. M. Fauchet, "Silicon photonic crystal nanocavity-coupled waveguides for error-corrected optical biosensing," Biosens. Bioelectron. **26**, 4024–4031 (2011).
24. S. Chakravarty, Y. Zou, W. Lai, and R. T. Chen, "Slow light engineering for high Q high sensitivity photonic crystal microcavity biosensors in silicon," Biosens. Bioelectron. **38**, 170–176 (2012).
25. M. S. Luchansky, and R. C. Bailey, "High-Q optical sensors for chemical and biological analysis," Anal. Chem. **84**, 793–821 (2012).
26. W. W. Shia and R. C. Bailey, "Single domain antibodies for the detection of ricin using silicon," Anal. Chem. **85**, 805–810 (2013).
27. S. Hachuda, S. Otsuka, S. Kita, T. Isono, M. Narimatsu, K. Watanabe, Y. Goshima, and T. Baba, "Selective detection of sub-atto-molar Streptavidin in 10^{1}3-fold impure sample using photonic crystal nanolaser sensors," Opt. Express **21**, 12815–12821 (2013).
28. V. R. Dantham, S. Holler, C. Barbre, D. Keng, V. Kolchenko, and S. Arnold, "Label-free detection of single protein using a nanoplasmonic-photonic hybrid microcavity," Nano Lett. **13**, 3347–3351 (2013).
29. S. Maestranzi, R. Przemioslo, H. Mitchell, and R. A. Sherwood, "The effect of benign and malignant liver disease on the tumour markers CA19-9 and CEA," Ann. Clin. Biochem. **35**, 99-103 (1998).
30. I. Langmuir, "The adsorption of gases on plane surface of glass, mica and platinum," The Research Laboratory of The General Electric Company: 1361–1402 (1918).
31. R. Abraham, S. Buxbaum, L. John, R. Smith, C. Venti, and D. Michael, "Screening and kinetic analysis of recombinant anti-CEA antibody fragments," J. Immunol. Meth. **183**, 119–125 (1995).

1. Introduction

With the discovery of new disease biomarkers and the emergence of new pathogenic strains of bacteria and viruses, rapid and sensitive bio-molecule detection is increasingly important in biomedicine and public health. Fluorescence based assays (e.g. enzyme-linked immunosorbent assay (ELISA), microarray [1–4]) have enabled a number of scientific advances and commercial applications. However, the labeling approaches are often difficult to control, can interfere with receptor affinity, can change protein dynamics, and cannot reveal the real-time dynamics. In this work, we develop a label-free protein chip based on photonic crystal nanobeam cavities [5]. This protein chip is capable of monitoring the binding process of proteins in real-time, with a sensitivity in the range of pg/mL. Furthermore, the chips are fabricated at a CMOS-compatible silicon photonics foundry at wafer scale, with an entirely scalable process. This shows great promise in not only high sensitivity protein detection, but also low-cost scalable production, thus, further opening the door for clinical and industrial applications.

2. Photonic crystal nanobeam cavities

The photonic crystal nanobeam cavity is a perforated silicon waveguide resting on a silicon dioxide substrate (Fig. 1(a)). The perforation is patterned periodically to tightly confine the light into the center of the structure via optical interference [5]. The protein detection is achieved by

#199338 - $15.00 USD Received 14 Oct 2013; revised 3 Dec 2013; accepted 4 Dec 2013; published 19 Dec 2013

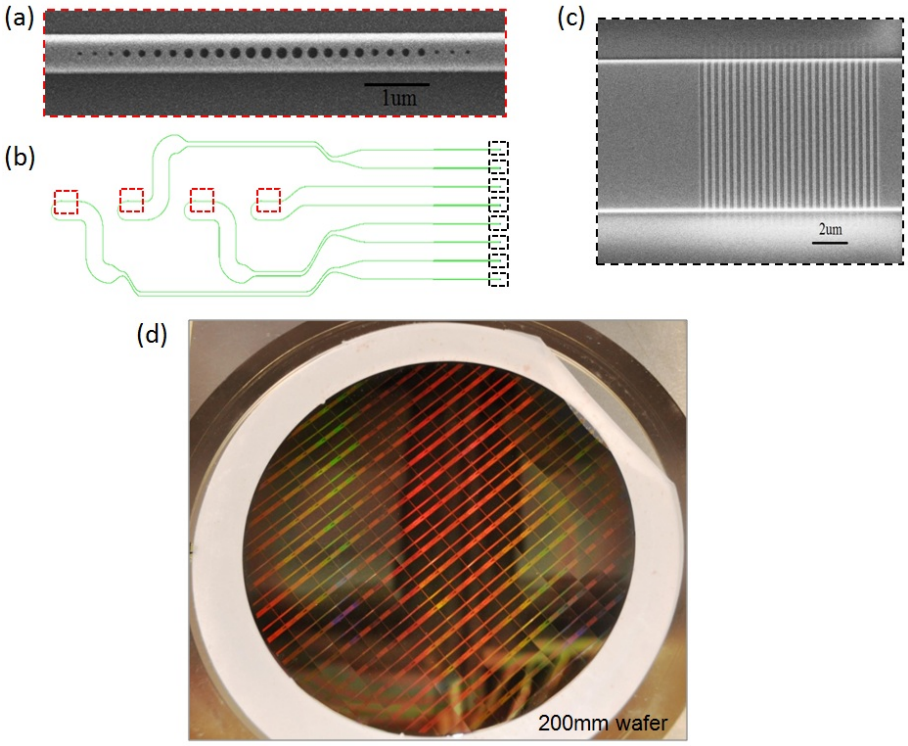

Fig. 1. (a) Scanning electron microscope (SEM) image of a photonic crystal nanobeam cavity. (b) Photonic circuits that consist of waveguides (green lines), cavities (in red boxes) and grating couplers (in black boxes). (c) SEM image of the grating coupler. (d) Photograph of the 200mm wafer, diced into ∼150 sensor chips.

monitoring the optical resonance of the cavity: the resonance wavelength will change when proteins bind to the surface of the cavity due to the increased refractive indices relative to the carrier fluid. The magnitude of resonance shift scales with the amount of proteins that are bound on the sensor surface and inversely scales with the size of the optical mode volume. In this work, we use the photonic crystal nanobeam cavity, taking advantage of its ultra-small optical mode volume [6]. Fabrication of nanobeam cavities is typically achieved by electron beam lithography (E-beam, with ∼5nm resolution) [7–12], however, the E-beam process is not scalable, thus limiting its capability for high volume production. In this work, we explore the possibility of fabricating chips in large quantities with scalable photolithography technology. The fabrication is processed in the IMEC-ePixfab micro-fabrication foundry. It provides wafer scale technologies based on deep UV (DUV) lithography with 193nm and 248nm exposure wavelengths. The benefits of DUV lithography are (1) fast process: the tool step-scans the mask and replicates the patterns of the mask to the wafer. Depending on the die size, 50 to 1000 chips per 200 mm wafer can be obtained in a couple of minutes. (2) low-cost: with DUV lithography, fabricating 1000 chips is almost the same as fabricating one, hence cost per chip reduces as the volume increases.

Figure 1(d) shows a photograph of the final wafer. The 200mm wafer was diced into ∼150 pieces, with each 12.36mm by 13.80mm. On each chip, an array of optical circuits were fabricated containing nanobeam photonic crystal cavities, optical waveguides and grating couplers (schematics shown in Fig. 1(b)). Figure 1(a) shows scanning electron micrograph (SEM) im-

#199338 - $15.00 USD Received 14 Oct 2013; revised 3 Dec 2013; accepted 4 Dec 2013; published 19 Dec 2013

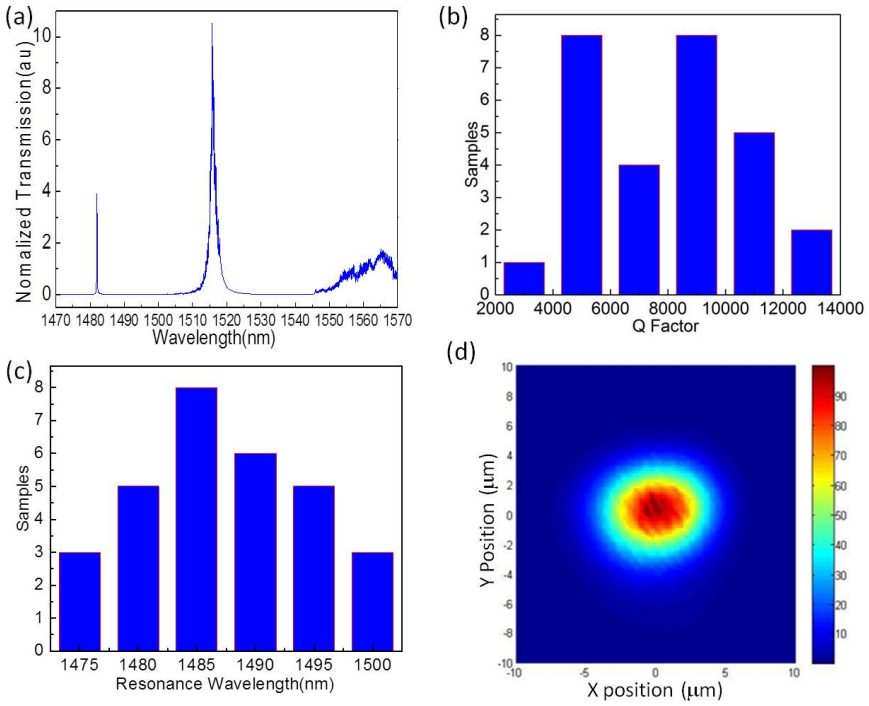

Fig. 2. (a) Transmission spectrum of the nanobeam cavity measured by scanning the tunable laser from 1470nm to 1570nm. The Q-factor of the fundamental mode (resonant at 1482nm in air) is 14,000 obtained by fitting to a Lorentzian line-shape. (b)&(c) Q-factors and resonance wavelengths of 28 samples, fabricated with different dosages in the range of (19 ± 1.6)mJ/cm^2. (d) Output signal normalized to its maximum as the fiber array is scanned around its optimal coupling position with 1550nm laser. Coupling decreases to the half-maximum value at $\pm 2\mu$m away from the center, displaying a high alignment tolerance.

age of the nanobeam cavity, the core sensing element. The nanobeam cavity is designed with the deterministic method that was demonstrated previously [13]. The holes are spaced with a periodicity of 340nm. The diameters of the holes are decreased from 210nm to 120nm with 20 gratings in a quadratic manner. With current UV photolithographic tools, only the first 13 gratings came out, while the rest failed either during the photolithography process or during the silicon etching process. Figure 1(c) shows the SEM image of the grating coupler. The distance between the two grating couplers is 250μm, designed to fit the commercial fiber arrays (OZ optics). In this scheme, two adjacent fibers from the fiber array were aligned with the grating coupler for in/out coupling. Previous work shows that the second order reflection occurring during coupling can be minimized by mounting the fiber array at 10° to the vertical [14]. For initial alignment, an objective was used to image the fiber position with respect to the grating. The fibers were located about 2mm above the grating, which results in low signal but easy alignment. The input wavelength was chosen at 1550nm - the designed center wavelength of the coupling. Once initial coupling was achieved, the fiber array was lowered to $\sim 20\mu m$ above the chip. The fiber array was situated on a 3-axis motorized stage, and an automated x-y position scan was performed to locate the optimal coupling. A tunable laser source was used to probe the transmission of the nanobeam cavity. Figure 2(a) shows the cavity spectrum. The funda-

#199338 - $15.00 USD Received 14 Oct 2013; revised 3 Dec 2013; accepted 4 Dec 2013; published 19 Dec 2013

mental cavity mode has resonance at 1482nm, with Q of 14,000 (in air), obtained by fitting to the Lorentzian profile.

To study the yield and fabrication tolerance, a total number of 28 samples were tested. These 28 samples were fabricated with a dosage sweep in the range of (19 ± 1.6)mJ/cm^2. Measured Q-factors are summarized in Fig. 2(b). A mean Q-factor on the order of 10^4 was obtained. Q value has a large distribution because a dosage scan was performed at different chips across the wafer. The resonance wavelength is spanned from 1470nm to 1505nm (Fig. 2(c)). We further studied the alignment tolerance of the system by fixing the source at 1550nm, and scanning the fiber array around its optimal coupling position. The coupling efficiency of the grating coupler at its optimal position was calculated to be 19% at 1550nm. Figure 2(b) indicates that the alignment tolerance is about $\pm 2\mu m$ (decreased by half of its maximum), which is greatly improved from the fiber-waveguide end-coupling method ($< 0.5\mu$m) [5]. This is a significant advantage for instrument automation, especially for point-of-care testing tools. Furthermore, the sensors can be placed in large quantities in a 2D array format or at arbitrary positions on the chip. The vertical coupling geometry is ideal for wafer-scale (or chip-scale) scanning.

3. Refractive index sensing

The analyte-induced cavity resonance shift falls into two categories: it can be a homogenous change of the background refractive index or an outstanding refractive index change on the sensor surface by protein binding. First, the sensor was characterized for sensitivity to the homogenous change of background index. A microfluidic channel was fabricated with polydimethylsiloxane (PDMS) using replica molding of an SU-8 template. The microfluidic channel has dimensions of 2mm by 100μm by 50μm (length, width, height) with two sub-millimeter holes, one at each end as an inlet and outlet for fluid delivery. Both the silicon chip and the PDMS channel were first treated by oxygen plasma and immediately aligned using a home-made microscope aligner, followed by a curing process at $70^{\circ}C$ for 3 hours. The microfuidic channel was further permanently sealed on the chip with epoxy. The resonance of the cavity was measured before and after DI water, methanol, acetone, ethanol and isopropyl alcohol (IPA) were injected into the sensor. Figure 3(a) shows a strong linear relation between the resonances of the sensor and the refractive indices of the solvents. A linear fitting results in a sensitivity of 69nm/RIU (RIU: refractive index unit). The refractive index sensitivity depends on the portion of the optical energy lying outside of silicon, and generally is in trade-off to its *Q*-factors [15]. The current design is optimized for high *Q*-factor and high fabrication tolerance, as UV-lithography was used in fabrication. A further optimized structure (but with more strict fabrication requirements) is demonstrated by Yang et. al. [16].

4. Biomarker detection by antigen-antibody reaction

The practically more meaningful application is to detect biomarkers that are captured on the sensor surface [17–28]. Since the cavity resonance shift inversely scales with the optical mode volume, the nanobeam cavity (with ultra-small mode volume on the wavelength scale) is an excellent platform to achieve high sensitivity for protein detection. Here we demonstrate the label-free detection of carcinoembryonic antigen (CEA) from 0.1pg/mL to 10ug/mL. CEA is a tumor biomarker and can be used to monitor the colon cancer treatment, and identify the recurrence after surgical resection [29].

The silicon chip was cleaned with acetone, methanol and IPA, then activated by oxygen plasma. The PDMS channel was also activated with oxygen plasma and bound, cured, and sealed with epoxy onto the chip. To selectively detect CEA, we used the antibody-antigen locking mechanism and modify the sensor surface as follows [18, 19]: First, a 2% solution of 3-aminopropyltrimethoxysilane (APTES) in 95% ethanol was injected into the microflu-

#199338 - $15.00 USD Received 14 Oct 2013; revised 3 Dec 2013; accepted 4 Dec 2013; published 19 Dec 2013

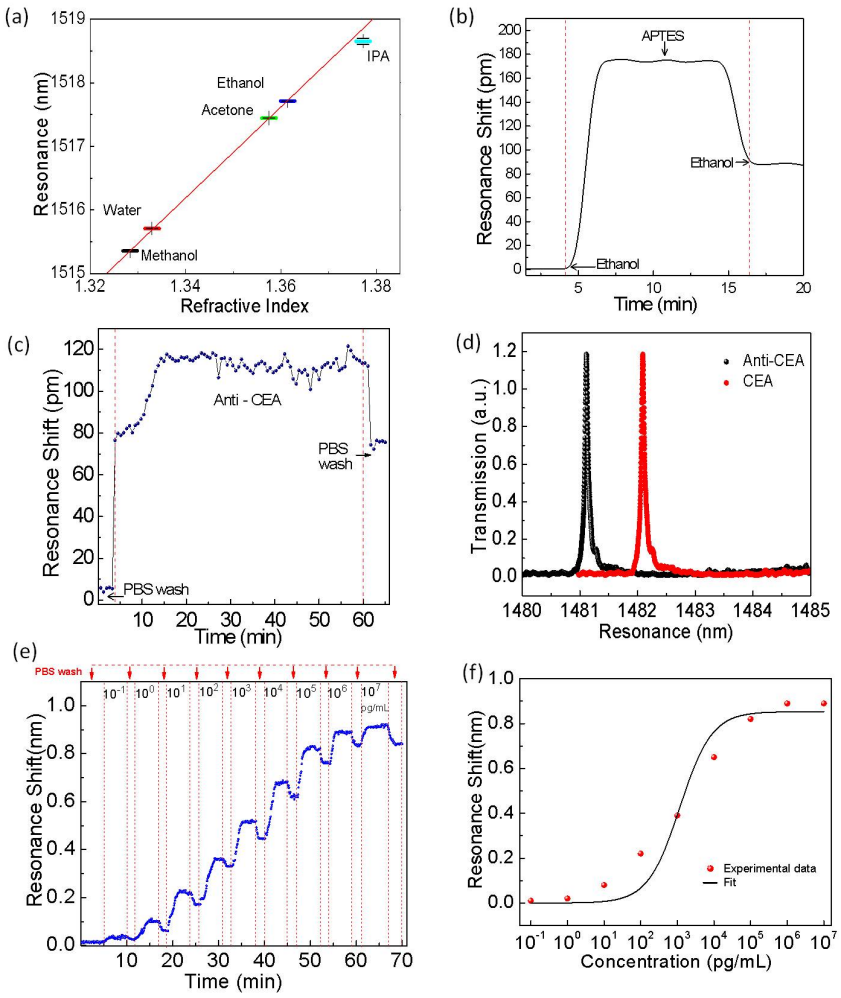

Fig. 3. (a) Liquids with different refractive indices (methanol, DI water, acetone, ethanol and isopropyl alcohol) were injected into the sensor. Resonance of the sensor v.s. their refractive indices displaces a linear relation. The red line is the linear fit. (b) Real-time resonance shifts as 3-aminopropyltrimethoxysilane (APTES) was injected into the channel, followed by wash with ethanol. (c) Real-time resonance shift as anti-CEA was bound on the sensor surface, followed by wash with PBS. (d) Resonance signal before and after the CEA sensing experiment. (e) Real-time resonance shift as different concentrations of CEA (0.1, 1, 10, 100pg/mL; 1, 10, 100ng/mL and 1, 10μg/mL in PBS) were consecutively injected into the channel. The red dotted line indicates each concentration, and the PBS-wash step between two consecutive concentrations. (f) Resonance shift v.s. concentration of CEA, and fitted with Langmuir equation. A dissociation constant of 14ng/mL is obtained from fitting.

#199338 - $15.00 USD Received 14 Oct 2013; revised 3 Dec 2013; accepted 4 Dec 2013; published 19 Dec 2013

idic channel for 10 minutes, followed by a removal of residual siloxane by flushing with 95% ethanol. The resonance shift during this process was monitored in real time (Fig. 3(b)), indicating the APTES had sufficiently reacted with the activated silicon surface. Next, 10mM of glutaraldehyde (Sigma) and 10mM of sodium cyanoborohydride (Sigma) pre-mixed solution were injected for 2 hours, followed by a wash with phosphate buffered saline (PBS). This created aldehyde termination on the sensor surface. Anti-CEA (1ug/mL) was subsequently injected for 1 hour and washed by PBS for 5 minutes. Figure 3(c) shows that anti-CEA was successfully captured on the sensor surface. Finally, different concentrations of CEA (0.1, 1, 10, 100pg/mL; 1, 10, 100ng/mL and 1, 10μg/mL in PBS) were consecutively injected to the microfluidic channel. The fluid rate was kept at 2μL/min, delivered by a syringe pump (Harvard Apparatus). Figure 3(d) shows the representative resonance curve before and after the CEA sensing experiment. Figure 3(e) shows the real time resonance shift during the sensing process, extracted by Lorentzian fitting. The red dotted line indicates different steps for different concentrations of CEA. A clear binding signal was observed starting from 10pg/mL. At concentrations above 1μg/mL, PBS wash brought the sensor resonance back to the baseline. This indicates that the sensor surface was saturated by antigen-antibody binding, and all excess shifts were due to physical absorption, which was washed off by PBS. In Fig. 3(f), we plotted resonance shift v.s. concentration of CEA, and fitted the curve with Langmuir equation [30]. From fitting, we obtained the dissociation constant of 14ng/mL, consistent with the results obtained by commercial label-free instruments [31].

5. Conclusion

In summary, we demonstrated the detection of CEA biomarker from 0.1pg/mL to 10μg/mL, over 8 orders of magnitude and achieving a detection limit of sub-pg/mL. The dissociation constant of CEA protein was also obtained from the concentration measurement. The sensor chips in our experiment were fabricated by scalable deep UV lithography and have shown high yield and high dose tolerance, with a mean Q factor of 9,000. The top-down fabrication approach also enables high density integration and interfacing between photonics and electronics. This shows great promise in achieving low-cost, high-sensitivity, and high-throughput automated biomedical point-of-care testing tools.

Acknowledgments

This work is supported in part by the Rowland Institute at Harvard and AFOSR Award FA9550-09-1-0669-DOD35CAP. The authors greatly acknowledge helpful discussions with D. L. Floyd.

#199338 - $15.00 USD Received 14 Oct 2013; revised 3 Dec 2013; accepted 4 Dec 2013; published 19 Dec 2013